ACSNANO

www.acsnano.org

ARTICLE

Rapid Biomarker Screening of Alzheimer's Disease by Interpretable Machine Learning and Graphene-Assisted Raman Spectroscopy

Ziyang Wang, Jiarong Ye, Kunyan Zhang, Li Ding, Tomotaroh Granzier-Nakajima, Jeewan C. Ranasinghe, Yuan Xue, Shubhang Sharma, Isabelle Biase, Mauricio Terrones, Se Hoon Choi, Chongzhao Ran, Rudolph E. Tanzi, Sharon X. Huang,* Can Zhang,* and Shengxi Huang*

Cite This: *ACS Nano* 2022, 16, 6426−6436

Read Online

ACCESS | Metrics & More | Article Recommendations | Supporting Information

ABSTRACT: **The study of Alzheimer's disease (AD), the most common cause of dementia, faces challenges in terms of understanding the cause, monitoring the pathogenesis, and developing early diagnoses and effective treatments. Rapid and accurate identification of AD biomarkers in the brain is critical to providing key insights into AD and facilitating the development of early diagnosis methods. In this work, we developed a platform that enables a rapid screening of AD biomarkers by employing graphene-assisted Raman spectroscopy and machine learning interpretation in AD transgenic animal brains. Specifically, we collected Raman spectra on slices of mouse brains with and without AD and used machine learning to classify AD and non-AD spectra. By contacting monolayer graphene with the brain slices, the accuracy was increased from 77% to 98% in machine learning classification. Further, using a linear support vector machine (SVM), we identified a spectral feature importance map that reveals the importance of each Raman wavenumber in classifying AD and non-AD spectra. Based on this spectral feature importance map, we identified AD biomarkers including Aβ and tau proteins and other potential biomarkers, such as triolein, phosphatidylcholine, and actin, which have been confirmed by other biochemical studies. Our Raman−machine learning integrated method with interpretability will facilitate the study of AD and can be extended to other tissues and biofluids and for various other diseases.**

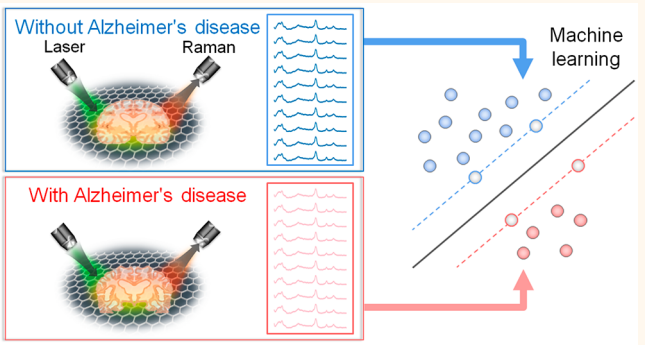

KEYWORDS: *Alzheimer's disease, graphene-assisted Raman spectroscopy, machine learning interpretation, signal-to-noise ratio, spectral feature importance*

INTRODUCTION

Alzheimer's disease (AD), a progressive disorder of the brain that causes memory losses, damages other brain functions, and is the most common cause of dementia.[1] By 2020, about 44 million people worldwide had been diagnosed with AD.[2] Despite the prevalence, the causes of AD are still not fully understood. Studying biomarkers related to AD greatly accelerates the understanding of the disease and can lead to new treatments against dementia.[3,4] Three biomarkers, T-tau, P-tau, and Aβ_{42}, have been identified and confirmed in the cerebrospinal fluid that are strongly associated with AD and could be used as progression markers in developing drugs.[5] To detect the AD-associated biomarkers in the brain, various imaging techniques have been developed, such as magnetic resonance imaging (MRI) and positron emission tomography (PET).[6−8] However, MRI and PET are costly and time-consuming while they still lack specific molecular information.[6,7] Other biosensing methods such as surface plasmon resonance biosensors and field-effect transistors offer specific information on the optical or electronic properties of the analyte[8−10] and, thus, are insufficient to gain comprehensive insights into the biomarkers of AD. Recently, spectroscopy based detection of AD biomarkers via immunoassay and fluorescence on blood and cerebrospinal fluid (CSF) has been intensively investigated in preclinical stages,[11−14] but they are

Received: January 17, 2022
Accepted: March 21, 2022
Published: March 25, 2022

https://doi.org/10.1021/acsnano.2c00538
ACS Nano 2022, 16, 6426−6436

not label-free, which prevents the discovery of novel biomarkers. New methods to rapidly screen and identify potential AD biomarkers from a huge number of candidate molecules are still urgently needed.

Raman spectroscopy is a nondestructive and label-free molecular sensing method. By exciting the samples with a monochromatic laser and collecting the inelastically scattered signal from the analyte, the obtained Raman spectrum provides the fingerprints of the analyte. Additionally, it offers high multiplexity and high specificity due to the multiple and extremely narrow Raman peaks. Since Raman spectroscopy provides a desirable approach with rapid diagnosis, it has been utilized to investigate AD in terms of diagnosing AD with Lewy bodies in blood plasma,[15] classifying early pathological states of AD with brain hippocampus regions,[6] imaging amyloid plaques in brain tissues,[16] *etc.* Despite the specificity, multiplexity, and rapid diagnosis, the interpretation of the Raman signals in complex biosamples is challenging. Although spectral comparison and principal component analysis (PCA) have been employed in Raman spectral analysis, molecule identification is unreliable when the intraclass spectral variation is too high.[17−21]

In recent years, machine learning has been frequently employed in Raman spectral analyses for disease diagnosis such as AD, cancer, infectious disease, *etc.*[22−25] High accuracy in diagnosis is enabled by machine learning models including support vector machine (SVM),[26] random forest,[27] and neural networks.[28] Besides achieving outstanding performance in classification, machine learning can also interpret the correlation between Raman modes and diseases by providing a spectral feature importance map.[29,30] Such interpretability of machine learning can lead to key insights into the potential disease biomarkers by correlating the spectral feature importance map with the signature molecular Raman spectra. However, so far, machine learning interpretation lacks quantitative correlation to the molecular composition in the Raman analysis for biomedical systems.[22−25]

In this work, we employed machine learning classification and interpretation on Raman spectra of mouse brain slices and screened AD biomarkers. Our workflow is primarily composed of three steps: first, we collected Raman spectra on mice brain slices with and without AD; then, we used machine learning to classify the collected Raman spectra on AD and non-AD brain slices; finally, we used linear SVM to interpret the spectral feature importance map which differentiates AD and non-AD spectra and discovered potential AD biomarkers (Figure 1). In our Raman measurements, we used a special noise reduction technique: contacting monolayer graphene with the brain slices. Compared to intrinsic Raman spectroscopy, our graphene-assisted Raman spectroscopy enhanced the Raman signal-to-noise ratios (from 53.9 to 121.0) and improved the machine learning classification performance (accuracy from 77% to 98%). By comparing the machine learning prediction accuracy on Raman spectra from different brain regions, our experiment revealed that certain brain regions, such as the cortex, are more informative in AD identification. In our machine learning interpretation, the spectral feature importance map is found to register well with the Raman signatures of known AD biomarkers, including Aβ and tau proteins. We also located several other molecules that have high Raman spectral correlation with the spectral feature importance map, which have been verified in previous biochemical studies, indicating their potential as biomarkers for AD diagnosis.

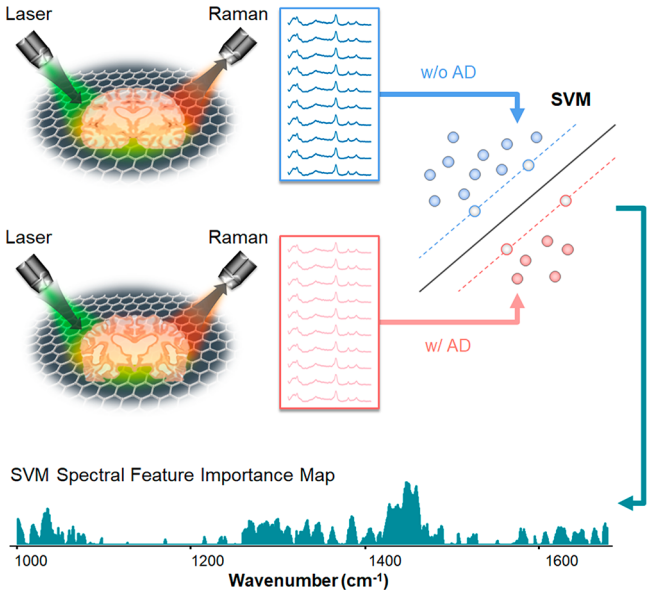

Figure 1. Overall workflow. Workflow of graphene-assisted Raman signals' data collection, preprocessing, and machine learning classification and interpretation. The machine learning classifier demonstrated is the linear SVM model to differentiate AD/non-AD Raman spectra.

Combining Raman sensing and machine learning analysis to enable biomarker identification on brain slices, our interpretable machine learning based framework provides a route for fundamental study of AD pathology and will facilitate AD diagnosis and drug development. Our Raman−machine learning integrated method has the potential to be extended to study other diseases and can be applied to various tissues, biofluids, and human samples.

RESULTS AND DISCUSSION

Improving the Signal-to-Noise Ratio Using Graphene-Assisted Raman Spectroscopy. We collected Raman spectra of brain slices harvested from AD transgenic mice and healthy mice. There are in total 351 spectra with AD and 376 spectra without AD in our data set measured on three brain regions: cortex, hippocampus, and thalamus. During the Raman measurement, the brain slices were immersed in a neuroprotectant solution sealed between the silicon substrate and a fused quartz cover slide. For part of the measurements, we placed brain slices in direct contact with monolayer graphene which had been transferred onto the quartz cover slide (Figure S1).

Before feeding the Raman spectra into machine learning classifiers, we implemented the Savitzky-Golay filter[31] for spectral smoothing and asymmetric least-squares smoothing[32] for baseline correction. Comparisons of raw Raman spectra before and after preprocessing are shown in Figures S2 and S3. Parts a and b of Figure 2 show examples of the preprocessed Raman spectra for AD and non-AD samples measured with and without graphene contact. As can be seen, there are major Raman peaks at 1038 cm^{-1}, 1088 cm^{-1}, 1283 cm^{-1}, 1312 cm^{-1}, 1439 cm^{-1}, and 1458 cm^{-1} (Figure 2a and b). The graphene G band is at 1589 cm^{-1}, noted as G (Figure 2a and Figure S4). The other Raman peaks are contributed by Aβ and tau proteins and major molecular components in the brain (Table 1). For example, the 1283 cm^{-1} mode is contributed by the

https://doi.org/10.1021/acsnano.2c00538
ACS Nano 2022, 16, 6426−6436

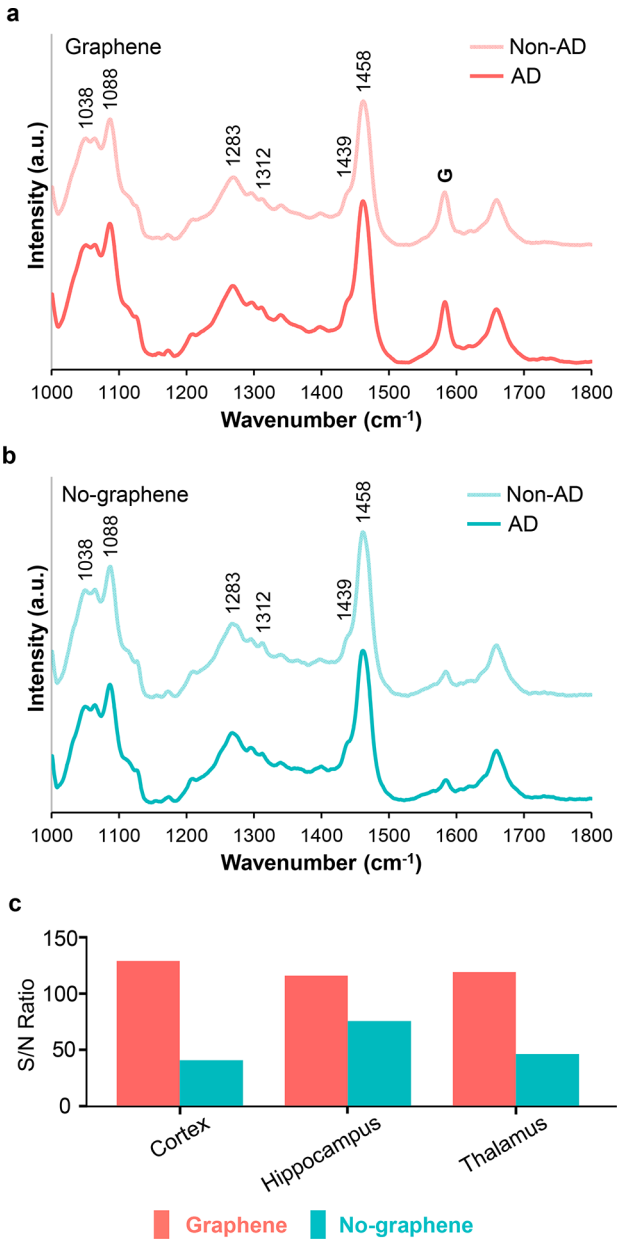

Figure 2. Raman spectra on brain slices. (a) Preprocessed Raman spectra in the cortex region with and without AD, with graphene. The graphene G-band at 1589 cm^{-1} is notated as "G′". (b) Preprocessed Raman spectra in the cortex region with and without AD, without graphene. (c) S/N of every brain region, measured with and without graphene.

CH_2 bending mode of oligomeric tau, actin, myelin basic protein, phosphatidylcholine, and triolein molecules. The Raman mode at 1458 cm^{-1} is contributed by the C−C stretching mode and CH_2 bending mode of oligomeric Aβ, oligomeric tau, actin, glycogen, lactate, phosphatidylcholine, and triolein molecules.

We calculated the signal-to-noise ratios (S/N) for spectra with and without graphene in three brain regions. The S/N are shown in Figure 2c, where red bars correspond to graphene-assisted spectra and blue bars represent the no-graphene results. It is clear that the graphene-assisted spectra exhibit much higher S/N than the no-graphene spectra for all the three brain regions (S/N average of 121.0 for graphene-assisted spectra compared to 53.9 for no-graphene spectra). Overall, we observed that when brain slices were placed in contact with graphene, the Raman spectra exhibited less noise when compared to the measurements without graphene. Our prior work, along with others, has shown that graphene can reduce the noise of Raman spectra, enhance Raman signals, and quench fluorescence for organic and biomolecules.[57−60] Here, the reduced noise can be attributed to the above factors, as well as the high thermal conductivity of graphene, which can reduce the laser heating effect during Raman measurements of brain slices.[61,62] Therefore, we used graphene-assisted Raman spectra for further investigations described in the following sections.

Table 1. Assignments of Most Important Raman Bands[a]

Peak position (cm^{-1})	Band assignment	Tentative contribution
1038	(C−O)[b]	Oligomeric Aβ, Fibril Aβ; Actin, Glycogen, Myelin basic protein
1063	(C−C)[b]	Oligomeric tau; Actin, Myelin basic protein, Phosphatidylcholine, Triolein
1088	(C−O−C)[b]	Aspartate aminotransferase, Ubiquitin
1270	Amide III	
1283	(CH_2)[c]	Oligomeric tau; Actin, Myelin basic protein, Phosphatidylcholine, Triolein
1297	(CH_2)[c]	Oligomeric Aβ; Actin
1312	(CH_2)[d]	Monomeric tau, Fibril tau; Actin, Glycogen, Myelin basic protein, Phosphatidylcholine, Triolein
1439	(CH_2)[c]	Monomeric Aβ, Oligomeric tau, Fibril tau; Aspartate aminotransferase, Lactate, Cholesterol, Myelin basic protein
1458	(C−C)[b], (CH_2)[c]	Oligomeric Aβ, Oligomeric tau; Actin, Glycogen, Lactate, Phosphatidylcholine, Triolein

[a]Raman vibration modes, Aβ and tau proteins, and 17 major composite molecules of the brain assigned to major Raman peaks.[6,33−56]. [b]Stretching. [c]Bending. [d]Twisting

Machine Learning Classification. In order to classify AD and non-AD spectra, we used the graphene-assisted spectra and applied different algorithms including linear SVM,[26] random forest,[27] XGBoost,[63] and CatBoost.[64] The common metrics for machine learning, including classification accuracy, area under the receiver operating characteristic curve (AUC), sensitivity, and specificity for graphene-assisted Raman spectra, are shown in Figure 3. Although the Raman spectra for AD and non-AD brain slices are visually similar (Figure 2a), machine learning classification can capture minor differences and distinguish the two classes with high accuracy. It can be seen from Figure 3 that the cortex region rendered the accuracy over 93% for every classifier. Compared to the hippocampus and thalamus, the cortex region exhibited better accuracy, AUC, sensitivity, and specificity for all classifiers. Thus, we can infer that the Raman fingerprints of AD-relevant biomarkers are better captured in the cortex region with graphene assistance.[65] It should be noted that our results do not indicate that the roles of hippocampus and thalamus in AD should be ignored since our observations only indicate that the graphene-assisted Raman signal is more sensitive to AD-relevant molecular components in the cortex region compared to the other two regions. We also performed the same machine learning classification for Raman spectra measured without graphene, and the results are shown in Figure S5 and Table S1.

As the graphene-assisted Raman signals from the cortex region yield better results in the machine learning classification,

https://doi.org/10.1021/acsnano.2c00538
ACS Nano 2022, 16, 6426−6436

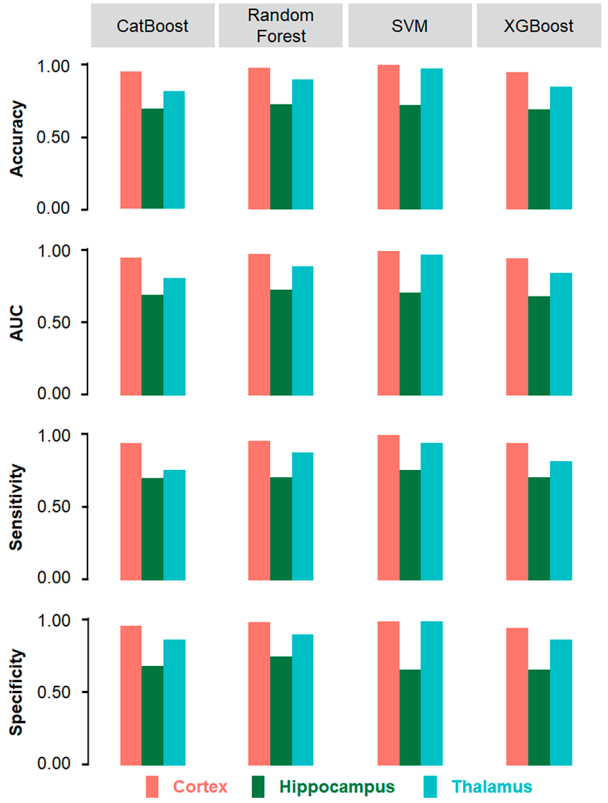

Figure 3. Machine learning classification summary on graphene-assisted Raman spectra. Accuracy, AUC, sensitivity, and specificity of graphene-assisted Raman spectra from the cortex, hippocampus, and thalamus regions.

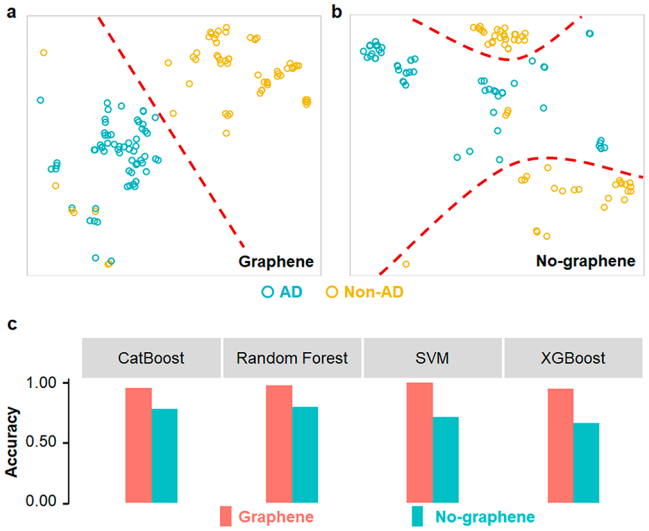

Figure 4. t-SNE plots for the cortex region. (a) t-SNE plot of graphene-assisted spectra on the cortex region. The red dashed line is the estimated linear decision boundary. (b) t-SNE plot of spectra without graphene on the cortex region. The red dashed curves are estimated nonlinear decision boundaries. (c) Comparison of classification accuracy between Raman spectra with and without graphene on the cortex region.

we visualized the data distribution using t-distributed stochastic neighbor embedding (t-SNE) plots, a nonlinear dimensionality reduction technique, for selecting appropriate interpretable machine learning classifiers.[66] As shown in Figure 4a, in the cortex region, the graphene-assisted Raman data can be well separated by a linear decision boundary while the Raman data measured without graphene are apparently not linearly separable (Figure 4b). Meanwhile, the machine learning classification accuracy using graphene-assisted Raman data reaches as high as 98% using linear SVM; however, the accuracy is at most 77% among the four classifiers using the no-graphene data (Figure 4c). This, again, shows the high quality of our graphene-assisted Raman data, which are more suitable for feature importance matching and interpretation (t-SNE plots from other brain regions are in Figure S6). A linear classifier with high accuracy is preferable to perform this interpretation task, since it is simple yet sufficient to fit the linearly separated data without introducing much model complexity, making its spectral feature map more straightforward for interpretation. Thus, we chose linear SVM from the series of tested machine learning models for further investigation to determine candidate biomarkers in association with AD.

Machine Learning Interpretation. We further interpreted the machine learning classification results and studied the features learned, which can provide important information on AD biomarker molecules. Validated by high accuracy, AUC, sensitivity, and specificity (Figure 3), the features learned by SVM from the graphene-assisted data in the cortex region are considered reliable for interpretation. From the trained linear SVM model, we assigned a spectral mapping of Raman wavenumbers based on their importance in classifying AD/non-AD spectra. The extracted spectral feature importance map contains two sets of features: positive features and negative features (positive features shown in Figure 5 and complete features shown in Figure S7). Since the spectral feature importance map shows the importance of each Raman wavenumber in the AD/non-AD classification, it stresses the difference between AD and non-AD Raman spectra.

As shown in Figure 5, the most important features from the machine learning interpretation are 1038, 1283, and 1458 cm^{-1}, whose importance values are 0.087, 0.056, and 0.15, respectively. All of these wavenumbers have Raman peaks for both AD and non-AD samples, but there is a slight difference: the AD samples exhibit about 10.5 ± 7.4%, 12.5 ± 3.5%, and 12.6 ± 1.4% stronger intensity than the non-AD samples, respectively, as shown in Figure 2a, which matches our analysis results that these wavenumbers possess important positive spectral features. The Raman mode at 1038 cm^{-1} may correspond to the C−O stretching mode in oligomeric Aβ and fibril Aβ proteins. It may also be contributed by actin, glycogen, and myelin basic protein molecules. The 1283 cm^{-1} peak may correspond to the CH_2 bending mode in oligomeric tau protein. It may also be contributed by actin, myelin basic protein, phosphatidylcholine, and triolein molecules. The 1458 cm^{-1} may correspond to the C−C stretching mode and CH_2 bending mode in oligomeric Aβ and oligomeric tau proteins. It may also be contributed by actin, phosphatidylcholine, and triolein molecules. The high spectral feature importance in those wavenumbers suggests that the biological molecules mentioned here are potentially related to the diagnosis of AD. On the other hand, if the Raman peaks identified in both AD and non-AD samples do not exhibit a significant spectral difference, the spectral feature importance does not necessarily show peaks in that wavenumber. For example, the graphene G band at 1589 cm^{-1} in both AD and non-AD spectra does not appear as an important wavenumber in Figure 5 since graphene

https://doi.org/10.1021/acsnano.2c00538
ACS Nano 2022, 16, 6426−6436

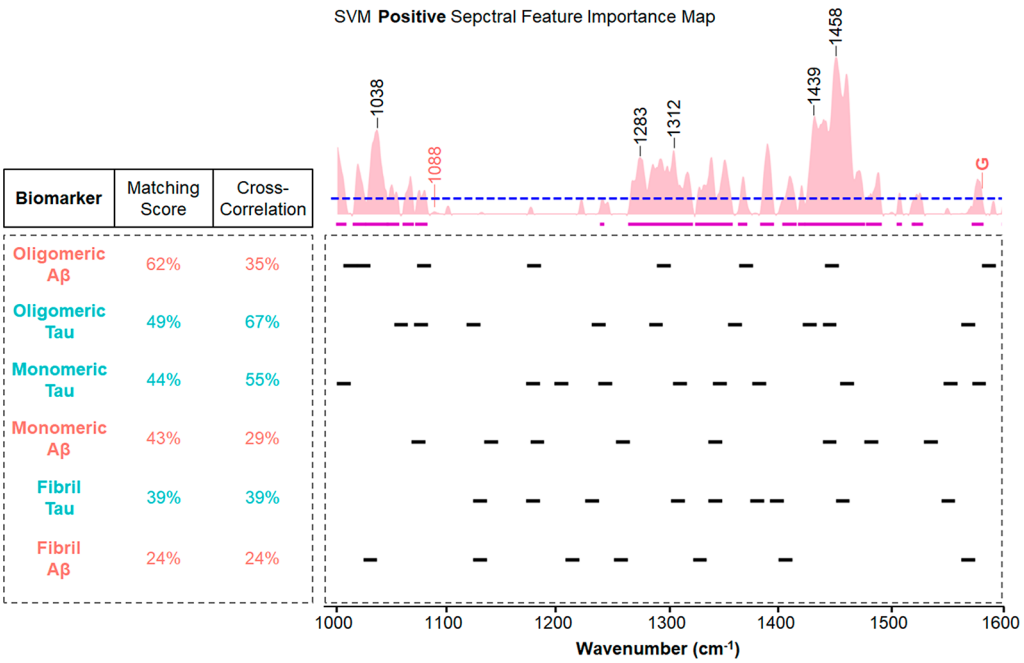

Figure 5. Feature importance matching for AD biomarkers. (Top) The positive spectral feature importance map found by SVM, where wavenumbers with high feature importance scores (*i.e.*, high values along the vertical axis) are important for AD recognition. On the spectral feature importance map, the blue dashed line is the threshold of the positive important feature ranges used for matching scores. The purple solid lines are important feature ranges above the threshold. Important peaks corresponding to signature Raman modes are labeled in black. Nonimportant peaks corresponding to signature Raman modes are differentiated in red. (Bottom left) The matching scores and cross-correlation coefficients between the SVM feature importance map and the previously reported six biomarkers.[51−53] (Bottom right) The black solid lines below the spectral feature importance map are the Raman signature peak ranges of six biomarkers with plus/minus 5 cm^{-1}. The wavenumber ranges from 1000 to 1600 cm^{-1}.

is deployed in the same way in both AD and non-AD samples. Also, the Raman peak around 1088 cm^{-1} for both AD and non-AD samples (Figure 2a), which is potentially related to the C−O−C stretching mode for aspartate aminotransferase and ubiquitin molecules, is not important according to our spectral feature importance, since the aspartate aminotransferase and ubiquitin molecules are not closely associated with AD. The interpretability of machine learning we demonstrated here presents an advantage of machine learning interpretation and enables the discovery of biomarkers that have very small quantities in the diseased samples, potentially allowing for early stage diagnosis and understanding of disease pathology.

To better understand our spectral feature importance map and its relationship with molecular components, we developed two metrics for two application scenarios: the Pearson cross-correlation coefficient based algorithm (if Raman spectra of biomarkers, including peak frequencies and intensities, are available) and the matching score based on spectral overlap between important feature ranges and biomarker Raman peaks (if only the peak frequencies of biomarkers are known and peak intensities are unavailable). Note that the former metric is relatively informative since it considers all spectral features including frequencies and intensities. On the other hand, the latter metric based only on peak frequency is relatively robust since peak frequency is stable compared with other spectral features such as intensity, which depends on the measurement conditions, such as the laser wavelength, laser power, and substrate. For validation, here we used both metrics to cross-check our interpretation results. We first examined several major AD biomarker proteins using both metrics. From the results shown in Figure 5, it is obvious that the known AD biomarkers such as oligomeric tau (with Raman peaks at 1063, 1283, 1439, and 1458 cm^{-1}, *etc.*) and oligomeric Aβ (with Raman peaks at 1038, 1297, and 1458 cm^{-1}, *etc.*) have considerable cross-correlation coefficients (Metric #1) and matching scores (Metric #2). To be more specific, oligomeric tau has a cross-correlation coefficient of 67% and a matching score of 49%, and oligomeric Aβ has a cross-correlation coefficient of 35% and a matching score of 62%, while other uncorrelated molecules such as tropomyosin and hemoglobin beta only have cross-correlation coefficients and matching scores no greater than 13%. Both of our metrics correctly identified the significance of Aβ and, meanwhile, recognized the role of tau in AD brain slices. This demonstrates the validity of the Pearson cross-correlation coefficient and matching score metrics that we developed.

Using the above two metrics, we can further screen more molecules that are potentially correlated to AD. We applied the cross-correlation coefficient and matching score to 17 major composite molecules of the brain (Table S2). The spectra of the component molecules with cross-correlation coefficients above 65% are shown in Figure 6. Triolein, phosphatidylcholine, and actin have the highest cross-correlation coefficients to the spectral feature importance map of 72%, 71%, and 69%, respectively. Consistent with the cross-correlation coefficient metric, the matching scores of these three molecules are also the highest among the 17 composite molecules. As clearly seen in Figure 6, the signature Raman peaks of the triolein molecule, phosphatidylcholine molecule, and actin molecule, including 1283 cm^{-1} (CH_2 bending mode), 1312 cm^{-1} (CH_2 twisting mode), and 1458 cm^{-1} (C−C stretching mode and CH_2 bending mode), match well with both our spectral feature

https://doi.org/10.1021/acsnano.2c00538
ACS Nano 2022, 16, 6426−6436

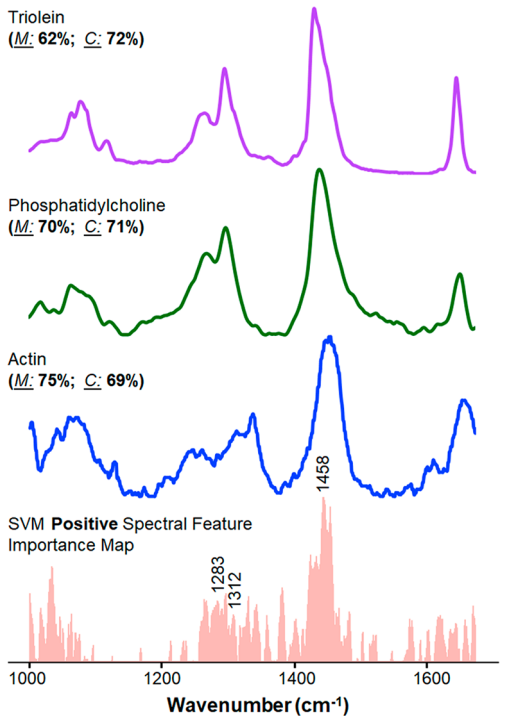

Figure 6. Other potential AD biomarkers identified. Biomolecular component spectra with the top three cross-correlation coefficients to the spectral feature importance map: triolein, phosphatidylcholine, and actin.[39,41,49] *M* refers to the matching score, and *C* refers to the cross-correlation coefficient.

importance map (Figure 6) and Raman peak analysis (Figure 2a and Table 1). This suggests that triolein, phosphatidylcholine, and actin may be associated with AD, which have been suggested by prior reports of biochemical and physiological studies.[67−69] For example, Bamburg et al. found an increase of actin in the AD brain compared to the normal brain.[67] Johnson et al. suggested that triglycerides, including triolein, can also lead to cognitive impairments, where they reported concentration levels of 46.49 mg/dl for AD animals and 35.01 mg/dl for healthy animals.[70] Banks et al. also showed that the decrease of triglycerides improves both learning and memory capabilities.[68] Additionally, phosphatidylcholine is found to be significantly lower in AD patients,[71] where high levels of phosphatidylcholine usually reduce the progression of dementia.[72] However, it is worth noting that the AD pathogenesis is different in mice and human brains in terms of the phosphatidylcholine level. According to Chan et al., phosphatidylcholine levels are lower in the AD human brain but higher in the mouse forebrain (18 mol% for AD animals and 16 mol% for healthy animals).[69]

In addition to the positive features shown in Figures 5 and 6, the SVM classifier also found negative features in the range 1100−1250 cm^{-1}, *i.e.*, the representative Raman spectral range for non-AD brain slices (Figure S7). This means that biomolecules with Raman peaks in this wavenumber range tend to be negatively correlated with AD (*i.e.* they likely reduce in amount or disappear with AD). These negative features correspond to cytochrome (with Raman peak at 1139 cm^{-1}) and glycogen (with Raman peak at 1237 cm^{-1}) in both matching metrics, suggesting that cytochrome and glycogen are negatively correlated to AD, again consistent with prior biochemical experiments.[73−76] In earlier studies, glycogen has been purposed to have beneficial effects for cognition,[73] whose negative correlation has been confirmed by Bass et al.[74] Furthermore, a decreased level of cytochrome has also been found in AD brain slices. For example, cytochrome c oxidase is found to decrease in AD as reported by Parker et al. and Cardoso et al.[75,76]

We note that our approach is able to screen potential biomarkers, rather than to accurately pinpoint all the biomarkers, which requires further biochemical verification. The accuracy of our matching score and cross-correlation coefficient metrics depends on the quality and range of molecular Raman data available in the literature. For instance, the matching score and cross-correlation coefficient values in Figures 5 and 6 are not directly comparable, because the Raman signal range used was 1000−1600 cm^{-1} for the results shown in Figure 5, and the Raman range used was 1000−1670 cm^{-1} for the results shown in Figure 6. The smaller Raman range for biomarker analysis (Figure 5) was due to the limited Raman spectral range reported for Aβ and tau proteins in the literature.[53] Although not reported before, Aβ and tau proteins might have many important Raman modes between 1600−1670 cm^{-1}, such as the amide I mode at 1665 cm^{-1} for the oligomer Aβ protein and the amide I mode at 1654 cm^{-1} for the fibril Aβ protein,[51,52] which could affect the matching scores and cross-correlation coefficients of Aβ and tau in our analysis. We further note that our biomarker screening method, in principle, is not limited by the number of biomarkers. To identify more potential biomarkers, we simply input the Raman spectra of other biomolecules within the same spectral range (*e.g.* from a Raman spectra database) in our component matching with spectral feature importance map.

CONCLUSION

In summary, we measured and analyzed Raman spectra on mice brain slices with and without AD and used machine learning to classify AD/non-AD spectra in order to screen biomarkers through the interpretation of spectral feature importance. Raman spectra, with their multiple and narrow Raman peaks, contain rich molecular information and potentially provide an ideal data set for machine learning analysis. Our graphene-assisted Raman measurements demonstrated further enhanced S/N and, thus, effectively improved the performance of the machine learning classification to achieve a high accuracy of 98%. To further interpret the molecular information in the Raman spectra, we obtained a spectral feature importance map based on our machine learning classifier and developed two metrics, including the cross-correlation coefficient and matching score, to identify molecules that are relevant to AD. Our interpretable machine learning based framework recognized a series of known AD biomarkers such as oligomeric tau and oligomeric Aβ that have a considerable correlation to AD. Our model also identified three molecules (triolein, phosphatidylcholine, and actin) that are positively correlated to AD and two molecules (cytochrome and glycogen) that are negatively correlated to AD. Our work offers a rapid approach to detect AD and to screen AD biomarker molecules; thus, it will facilitate the study of AD in terms of diagnosis and treatment. Our approach integrating graphene-assisted Raman spectroscopy and interpretable machine learning can also be widely applied to study various other diseases and to a wide range of biological samples including tissues and biofluids.

https://doi.org/10.1021/acsnano.2c00538
ACS Nano 2022, 16, 6426−6436

METHODS

Animals and Brain Slice Preparation. Animal investigation procedures were conducted in accordance with institutional and NIH guidelines. The animals were housed with *ad libitum* access to food and water in a room with a 12-h light and dark cycle in the animal facility. We utilized the previously reported 5XFAD mouse model expressing $APP^{Swedish/Florida/London}$ and $PSEN1^{M146L/L286V}$ mutations,[77,78] which recapitulates the features of Alzheimer's β-amyloid pathology in animal brains. 5XFAD mice of different ages and nontransgenic (non-AD) control mice were investigated. All animal study procedures were approved by MGH IACUC (Protocol #: 2011N000022).

Brain slices were prepared following previously reported methods.[79,80] Particularly, animals were anesthetized with isoflurane and then decapitated. Isolated brains were longitudinally bisected, and hemispheres were separated and incubated in 4% paraformaldehyde-containing 0.1 M phosphate-buffered saline (PBS) at 4 °C for 48 h, followed by incubation in 30% sucrose solution in 0.1 M PBS. Next, brains were snap frozen from a dry ice-cooled block on a sliding microtome (Leica SM 2010R) and sectioned in 40 μm thickness. The free-floating brain sections were stored at −20 °C in a cryoprotective buffer containing 28% ethylene glycol, 23% glycol, and 0.05 M PBS, until subsequent analysis by Raman testing.

Raman Measurement. Raman measurement was performed on the Horiba LabRam system with a 50× objective. The laser power on the sample was controlled below 0.4 mW to avoid potential laser bleaching. The excitation laser wavelength was 532.5 nm. All the measurements were performed on mice brain slices in the neuroprotectant solution that was sealed between a quartz cover slide and the silicon substrate. In the case with graphene in contact, the quartz slide has monolayer graphene transferred on the surface. In each Raman measurement, we carried out three accumulations; thus, each spectrum is, in effect, averaged three times.

Graphene Synthesis and Transfer. The graphene layers were synthesized by the chemical vapor deposition method. For the graphene growth, Cu foil was first placed in a quartz tube furnace and annealed at 1065 °C for 1 h under 60 sccm H_2 and 940 sccm Ar at atmospheric pressure. For the growth, the furnace was brought down to 1000 °C, and the gas flow rates were updated to 36 sccm H_2 and 2204 sccm Ar. Then, 0.6 sccm CH_4 was introduced for 1 h. After 1 h, the CH_4 was turned off and the Cu foil was rapidly cooled by removing it from the furnace area.

For the transfer, a supporting PMMA layer was spin-coated on top of the graphene/Cu stack. Then the Cu was etched away using a commercial Cu etchant. After the Cu has etched, the PMMA/graphene was put into three separate water baths for several hours, before being transferred to the desired final substrate. After the sample had dried, it was placed into acetone overnight in order to remove the PMMA and then rinsed with isopropyl alcohol and blow dried.

Data Preprocessing and Calculation of Signal-to-Noise Ratio. After obtaining the raw data, it is essential to apply preprocessing methods to reduce the effect of noise and background on classifiers. For each spectrum, we applied a Savitzky-Golay filter to reduce the spectral noise.[31] We removed the background using baseline correction with asymmetric least-squares smoothing.[32] To calculate S/N, we selected peaks of interest at 1038, 1088, 1283, 1458, and 1649 cm^{-1}. Then, we divided the average intensity of each peak by the standard deviation of the peak intensity across different AD spectra from the same brain region to calculate the S/N for a single peak. Finally, we averaged the S/N of all peaks of interest to get the S/N of spectra of the area. Notice that since we used the same preprocessing for all (both graphene and no-graphene) spectra, comparison between S/N of graphene and no-graphene spectra is not affected.

Classifiers' Architecture and Feature Importance. As shown in Figure 3, multiple classifiers were used in the experiment, including linear SVM, random forest, XGBoost, and CatBoost. Classification experiments were implemented using stratified 5-fold cross-validation to preserve the same percentage of samples for each class to improve robustness. For experiments with a relatively small sample set, SVM is usually an efficient and reliable option, for it is designed to find the optimal decision boundary represented by a hyperplane that maximizes the margin of separation between different classes.[24] In our binary classification, we used linear SVM to find the optimal linear decision boundary between the two classes. The sign of a feature weight obtained from the linear SVM classifier represents that feature's direction to predict class.[81,82] Hence, the feature weights can be intuitively interpreted as the spectral feature importance map shown in Figure 5 (positive only), while the positive (negative) features correspond to the Raman signals more represented in AD (non-AD) samples. We used the scikit-learn package to implement linear SVM and extract the spectral feature importance map.[83]

Component Cross-Correlation Coefficient for Raman. The Pearson correlation coefficient measures the linear correlation between two variables.[84] The method is a standard measure of similarity between two Raman spectra.[85] Here, we used the cross-correlation coefficient to measure the levels of correlation between the machine-learning-derived feature map and the Raman spectra of 17 commonly known components in the brain from the literature (Table S2).[33−48] We modified the Pearson cross-correlation coefficient method and excluded negatively correlated trends as shown as follows:

$$r_{xy} = \frac{\sum_{i=0}^{n} \max(0, (x_i - \bar{x})(y_i - \bar{y}))}{\sqrt{\sum_{i=0}^{n} (x_i - \bar{x})^2} \sqrt{\sum_{i=0}^{n} (y_i - \bar{y})^2}} \quad (1)$$

Considering the range difference of each spectrum, we normalized the components' spectra and the spectral feature importance map so that they were within the same interval (1000−1600 cm^{-1}) and have the same dimensions. Then we used eq 1 to calculate the cross-correlation coefficient. This results in a coefficient that ranges from [0, 1] where $r = 0$ means no correlation and $r = 1$ means perfect correlation.

Matching Score between the Machine-Learning-Derived Feature Map and Biomolecule Raman Spectra. Raman peak intensities vary with a number of factors, including excitation wavelength and substrate. To avoid the influence of Raman peak intensity variation, we developed another metric, the matching score, for measuring the correlation between biomarkers and distinguishable patterns learned from machine learning models to some extent. The metric is designed as a ratio, with the numerator as the sum of important feature ranges of the extracted feature map of a particular class (*i.e.* either AD or no AD) that overlap with Raman spectral peak ranges of a certain biomarker and the sum of the aforementioned biomarker peak ranges as the denominator. Significant Raman peak ranges of six biomarkers (Fibril tau, Fibril Aβ, oligomeric tau, oligomeric Aβ, monomeric tau, and ,onomeric Aβ) that are commonly known to be present in brain slides are gathered from the literature.[51−53] As demonstrated in Figure 5, Raman peak ranges are constructed by granting a shift of five wavenumbers for each biomarker representing important feature regions, the sum of which is utilized as the denominator for further calculations. Similarly, pinpointing the important feature ranges for the feature map as the numerator is also desired. Rather than extracting peaks from the feature map, we applied a 40% percentile threshold as the cutoff; regions above this we considered as significant, and we used the sum of their intersection with the denominator as the numerator. Matching scores of all six biomarkers and the positive feature map extracted from linear SVM training are presented in Figure 5, indicating that results from our matching score approach are consistent with biomedical findings using other methods.

ASSOCIATED CONTENT

Supporting Information

The Supporting Information is available free of charge at https://pubs.acs.org/doi/10.1021/acsnano.2c00538.

https://doi.org/10.1021/acsnano.2c00538
ACS Nano 2022, 16, 6426−6436

Additional figures and tables, including illustration of graphene-assisted Raman spectroscopy measurement, Raman spectra on brain slices before and after preprocessing, Raman spectra on brain slices after preprocessing, comparison between Raman spectra in the cortex region and graphene peaks, machine learning classification summary on no-graphene Raman spectra, t-SNE plots for thalamus and hippocampus regions, feature importance maps by linear SVM, random forest and XGBoost, numeric machine learning classification summary on both graphene-assisted and no-graphene Raman spectra, and 17 major composite molecules of the brain and their corresponding literature.

AUTHOR INFORMATION

Corresponding Authors

Sharon X. Huang − *College of Information Sciences and Technology, The Pennsylvania State University, University Park, Pennsylvania 16802, United States*

Can Zhang − *Genetics and Aging Research Unit, McCance Center for Brain Health, MassGeneral Institute for Neurodegenerative Disease Department of Neurology, Massachusetts General Hospital, Harvard Medical School, Charlestown, Massachusetts 02129, United States;* orcid.org/0000-0002-4340-5118

Shengxi Huang − *Department of Electrical Engineering, The Pennsylvania State University, University Park, Pennsylvania 16802, United States;* orcid.org/0000-0002-3618-9074

Authors

Ziyang Wang − *Department of Electrical Engineering, The Pennsylvania State University, University Park, Pennsylvania 16802, United States;* orcid.org/0000-0003-1368-4539

Jiarong Ye − *College of Information Sciences and Technology, The Pennsylvania State University, University Park, Pennsylvania 16802, United States*

Kunyan Zhang − *Department of Electrical Engineering, The Pennsylvania State University, University Park, Pennsylvania 16802, United States;* orcid.org/0000-0002-6830-409X

Li Ding − *Department of Electrical Engineering, The Pennsylvania State University, University Park, Pennsylvania 16802, United States*

Tomotaroh Granzier-Nakajima − *Department of Physics, The Pennsylvania State University, University Park, Pennsylvania 16802, United States*

Jeewan C. Ranasinghe − *Department of Electrical Engineering, The Pennsylvania State University, University Park, Pennsylvania 16802, United States*

Yuan Xue − *Department of Electrical and Computer Engineering, Johns Hopkins University, Baltimore, Maryland 21218, United States*

Shubhang Sharma − *Department of Computer Science, The Pennsylvania State University, University Park, Pennsylvania 16802, United States*

Isabelle Biase − *Department of Computer Science, The Pennsylvania State University, University Park, Pennsylvania 16802, United States*

Mauricio Terrones − *Department of Physics, The Pennsylvania State University, University Park, Pennsylvania 16802, United States;* orcid.org/0000-0003-0010-2851

Se Hoon Choi − *Genetics and Aging Research Unit, McCance Center for Brain Health, MassGeneral Institute for Neurodegenerative Disease Department of Neurology, Massachusetts General Hospital, Harvard Medical School, Charlestown, Massachusetts 02129, United States*

Chongzhao Ran − *Martinos Center for Biomedical Imaging, Massachusetts General Hospital, Harvard Medical School, Charlestown, Massachusetts 02129, United States;* orcid.org/0000-0002-3892-4108

Rudolph E. Tanzi − *Genetics and Aging Research Unit, McCance Center for Brain Health, MassGeneral Institute for Neurodegenerative Disease Department of Neurology, Massachusetts General Hospital, Harvard Medical School, Charlestown, Massachusetts 02129, United States*

Complete contact information is available at: https://pubs.acs.org/10.1021/acsnano.2c00538

Author Contributions

Z.W., J.Y., L.D., and J.R. performed experiments and analyzed data. T.G.-N. and M.T. synthesized graphene. Y.X., S.S., and I.B. helped with data analysis. S.H.C., C.R., R.E.T., and C.Z. engaged in animal studies and interpreted results of brain slices. S.X.H., C.Z., and S.H. designed and supervised the work. Z.W., J.Y., and K.Z. wrote the manuscript draft and prepared the figures. All authors reviewed and revised the manuscript to its final state.

Funding

The authors thank the Imaging Facility of Materials Characterization Lab at Penn State for instrument use. C.Z. and S.H. acknowledge the support from the National Institutes of Health under grant number R56AG062208. L.D. and S.H. acknowledge the support from Johnson & Johnson Inc. for the STEM2D Scholar's Award. S.H. acknowledges the support from the National Science Foundation under grant number ECCS-1943895. C.Z. acknowledges the support from the National Institutes of Health under grant number R01AG055784. C.Z. and R.E.T. acknowledge the support from the Cure Alzheimer's Fund.

Notes

Prior to submission, a preprint version of this article had been made available as Wang, Z.; Ye, J.; Zhang, K.; Ding, L.; Granzier-Nakajima, T.; Ranasinghe, J.; Xue, Y.; Sharma, S.; Biase, I.; Terrones, M.; Choi, S. H.; Ran, C.; Tanzi, R. E.; Huang, S. X.; Zhang, C.; Huang, S. Rapid Biomarker Screening of Alzheimer's Disease by Interpretable Machine Learning and Graphene-Assisted Raman Spectroscopy. *bioRxiv.* 2021, 2021.06.03.446929. https://www.biorxiv.org/content/10.1101/2021.06.03.446929 (last accessed 2022-03-16).

The authors declare no competing financial interest.

REFERENCES

(1) Burns, A.; Iliffe, S. Alzheimer's Disease. *BMJ* **2009**, *338*, b158.

(2) Sawda, C.; Moussa, C.; Turner, R. S. Resveratrol for Alzheimer's Disease. *Ann. N.Y. Acad. Sci.* **2017**, *1403* (1), 142.

(3) Blennow, K.; Zetterberg, H. Biomarkers for Alzheimer's Disease: Current Status and Prospects for the Future. *J. Int. Med.* **2018**, *284* (6), 643−663.

(4) Zetterberg, H.; Bendlin, B. B. Biomarkers for Alzheimer's Disease-Preparing for a New Era of Disease-Modifying Therapies. *Mol. Psychiatry* **2021**, *26* (1), 296−308.

(5) Olsson, B.; Lautner, R.; Andreasson, U.; Öhrfelt, A.; Portelius, E.; Bjerke, M.; Hölttä, M.; Rosén, C.; Olsson, C.; Strobel, G.; Wu, E.; Dakin, K.; Petzold, M.; Blennow, K.; Zetterberg, H. CSF and Blood Biomarkers for the Diagnosis of Alzheimer's Disease: A Systematic Review and Meta-Analysis. *Lancet Neurol.* **2016**, *15* (7), 673−684.

(6) Chen, P.; Shen, A.; Zhao, W.; Baek, S.-J.; Yuan, H.; Hu, J. Raman Signature from Brain Hippocampus Could Aid Alzheimer's Disease Diagnosis. *Appl. Opt.* **2009**, *48* (24), 4743−4748.
(7) Márquez, F.; Yassa, M. A. Neuroimaging Biomarkers for Alzheimer's Disease. *Mol. Neurodegener.* **2019**, *14* (1), 21.
(8) Aguilar, M.-I.; Small, D. H. Surface Plasmon Resonance for the Analysis of Beta-Amyloid Interactions and Fibril Formation in Alzheimer's Disease Research. *Neurotox. Res.* **2005**, *7* (1−2), 17−27.
(9) Lee, J.-H.; Kang, D.-Y.; Lee, T.; Kim, S.-U.; Oh, B.-K.; Choil, J.-W. Signal Enhancement of Surface Plasmon Resonance Based Immunosensor Using Gold Nanoparticle-Antibody Complex for Beta-Amyloid (1−40) Detection. *J. Nanosci. Nanotechnol.* **2009**, *9* (12), 7155−7160.
(10) Bungon, T.; Haslam, C.; Damiati, S.; O'Driscoll, B.; Whitley, T.; Davey, P.; Siligardi, G.; Charmet, J.; Awan, S. A. Graphene FET Sensors for Alzheimer's Disease Protein Biomarker Clusterin Detection. *Front Mol. Biosci* **2021**, *8*, 651232.
(11) Molinuevo, J. L.; Ayton, S.; Batrla, R.; Bednar, M. M.; Bittner, T.; Cummings, J.; Fagan, A. M.; Hampel, H.; Mielke, M. M.; Mikulskis, A.; O'Bryant, S.; Scheltens, P.; Sevigny, J.; Shaw, L. M.; Soares, H. D.; Tong, G.; Trojanowski, J. Q.; Zetterberg, H.; Blennow, K. Current State of Alzheimer's Fluid Biomarkers. *Acta Neuropathol.* **2018**, *136* (6), 821−853.
(12) Shi, L.; Lu, L.; Harvey, G.; Harvey, T.; Rodríguez-Contreras, A.; Alfano, R. R. Label-Free Fluorescence Spectroscopy for Detecting Key Biomolecules in Brain Tissue from a Mouse Model of Alzheimer's Disease. *Sci. Rep.* **2017**, *7* (1), 2599.
(13) Shin, J.; Park, S.; Lee, H.; Kim, Y. Thioflavin-Positive Tau Aggregates Complicating Quantification of Amyloid Plaques in the Brain of 5XFAD Transgenic Mouse Model. *Sci. Rep.* **2021**, *11* (1), 1617.
(14) Jun, Y. W.; Cho, S. W.; Jung, J.; Huh, Y.; Kim, Y.; Kim, D.; Ahn, K. H. Frontiers in Probing Alzheimer's Disease Biomarkers with Fluorescent Small Molecules. *ACS Cent Sci.* **2019**, *5* (2), 209−217.
(15) Paraskevaidi, M.; Morais, C. L. M.; Halliwell, D. E.; Mann, D. M. A.; Allsop, D.; Martin-Hirsch, P. L.; Martin, F. L. Raman Spectroscopy to Diagnose Alzheimer's Disease and Dementia with Lewy Bodies in Blood. *ACS Chem. Neurosci.* **2018**, *9* (11), 2786−2794.
(16) Ji, M.; Arbel, M.; Zhang, L.; Freudiger, C. W.; Hou, S. S.; Lin, D.; Yang, X.; Bacskai, B. J.; Xie, X. S. Label-Free Imaging of Amyloid Plaques in Alzheimer's Disease with Stimulated Raman Scattering Microscopy. *Sci. Adv.* **2018**, *4* (11), No. eaat7715.
(17) Lochocki, B.; Morrema, T. H. J.; Ariese, F.; Hoozemans, J. J. M.; de Boer, J. F. The Search for a Unique Raman Signature of Amyloid-Beta Plaques in Human Brain Tissue from Alzheimer's Disease Patients. *Analyst* **2020**, *145* (5), 1724−1736.
(18) Ong, Y. H.; Lim, M.; Liu, Q. Comparison of Principal Component Analysis and Biochemical Component Analysis in Raman Spectroscopy for the Discrimination of Apoptosis and Necrosis in K562 Leukemia Cells. *Opt. Express* **2012**, *20* (20), 22158−22171.
(19) Tong, D.; Chen, C.; Zhang, J.; Lv, G.; Zheng, X.; Zhang, Z.; Lv, X. Application of Raman Spectroscopy in the Detection of Hepatitis B Virus Infection. *Photodiagnosis Photodyn. Ther.* **2019**, *28*, 248−252.
(20) Chen, C.; Yang, L.; Zhao, J.; Yuan, Y.; Chen, C.; Tang, J.; Yang, H.; Yan, Z.; Wang, H.; Lv, X. Urine Raman Spectroscopy for Rapid and Inexpensive Diagnosis of Chronic Renal Failure (CRF) Using Multiple Classification Algorithms. *Optik* **2020**, *203*, 164043.
(21) Li, S.; Zhang, Y.; Xu, J.; Li, L.; Zeng, Q.; Lin, L.; Guo, Z.; Liu, Z.; Xiong, H.; Liu, S. Noninvasive Prostate Cancer Screening Based on Serum Surface-Enhanced Raman Spectroscopy and Support Vector Machine. *Appl. Phys. Lett.* **2014**, *105* (9), 091104.
(22) Ryzhikova, E.; Ralbovsky, N. M.; Sikirzhytski, V.; Kazakov, O.; Halamkova, L.; Quinn, J.; Zimmerman, E. A.; Lednev, I. K. Raman Spectroscopy and Machine Learning for Biomedical Applications: Alzheimer's Disease Diagnosis Based on the Analysis of Cerebrospinal Fluid. *Spectrochim. Acta A Mol. Biomol. Spectrosc.* **2021**, *248*, 119188.
(23) Ralbovsky, N. M.; Halámková, L.; Wall, K.; Anderson-Hanley, C.; Lednev, I. K. Screening for Alzheimer's Disease Using Saliva: A New Approach Based on Machine Learning and Raman Hyperspectroscopy. *J. Alzheimers. Dis.* **2019**, *71* (4), 1351−1359.
(24) Li, S.; Guo, Z.; Liu, Z. Surface-Enhanced Raman Spectroscopy + Support Vector Machine: A New Noninvasive Method for Prostate Cancer Screening? *Expert Rev. Anticancer Ther.* **2015**, *15* (1), 5−7.
(25) Khan, S.; Ullah, R.; Khan, A.; Ashraf, R.; Ali, H.; Bilal, M.; Saleem, M. Analysis of Hepatitis B Virus Infection in Blood Sera Using Raman Spectroscopy and Machine Learning. *Photodiagnosis Photodyn. Ther.* **2018**, *23*, 89−93.
(26) Zhang, Y. Support Vector Machine Classification Algorithm and Its Application. *Information Computing and Applications*; Springer Berlin Heidelberg, 2012; pp 179−186.
(27) Breiman, L. Random Forests. *Mach. Learn.* **2001**, *45* (1), 5−32.
(28) Lapedes, A.; Farber, R. How Neural Nets Work. *Evolution, Learning and Cognition*; World Scientific, 1989; pp 331−346.
(29) Putin, E.; Mamoshina, P.; Aliper, A.; Korzinkin, M.; Moskalev, A.; Kolosov, A.; Ostrovskiy, A.; Cantor, C.; Vijg, J.; Zhavoronkov, A. Deep Biomarkers of Human Aging: Application of Deep Neural Networks to Biomarker Development. *Aging* **2016**, *8* (5), 1021−1033.
(30) Huynh-Thu, V. A.; Saeys, Y.; Wehenkel, L.; Geurts, P. Statistical Interpretation of Machine Learning-Based Feature Importance Scores for Biomarker Discovery. *Bioinformatics* **2012**, *28* (13), 1766−1774.
(31) Savitzky, A.; Golay, M. J. E. Smoothing and Differentiation of Data by Simplified Least Squares Procedures. *Anal. Chem.* **1964**, *36* (8), 1627−1639.
(32) Eilers, P. H. C.; Boelens, H. F. M. Baseline Correction with Asymmetric Least Squares Smoothing. *Leiden University Medical Centre Report* **2005**, *1* (1), 5.
(33) Frushour, B. G.; Koenig, J. L. Raman Spectroscopic Study of Tropomyosin Denaturation. *Biopolymers* **1974**, *13* (9), 1809−1819.
(34) Kalkura, S. N.; Ramakrishnan, V.; Devanarayanan, S. IR and Raman Studies of Cholesterol Monohydrate Grown in Gel Medium. *Infrared Phys.* **1987**, *27* (5), 335−337.
(35) Maiti, N. C.; Apetri, M. M.; Zagorski, M. G.; Carey, P. R.; Anderson, V. E. Raman Spectroscopic Characterization of Secondary Structure in Natively Unfolded Proteins: α-Synuclein. *J. Am. Chem. Soc.* **2004**, *126* (8), 2399−2408.
(36) Kitagawa, T.; Kyogoku, Y.; Iizuka, T.; Ikeda-Saito, M.; Yamanaka, T. Resonance Raman Scattering from Hemoproteins. *J. Biochem.* **1975**, *78* (4), 719−728.
(37) Tuma, R. Raman Spectroscopy of Proteins: From Peptides to Large Assemblies. *J. Raman Spectrosc.* **2005**, *36* (4), 307−319.
(38) Syme, C. D.; Blanch, E. W.; Holt, C.; Jakes, R.; Goedert, M.; Hecht, L.; Barron, L. D. A Raman Optical Activity Study of Rheomorphism in Caseins, Synucleins and Tau. New Insight into the Structure and Behaviour of Natively Unfolded Proteins. *Eur. J. Biochem.* **2002**, *269* (1), 148−156.
(39) Bergholt, M. S.; Zheng, W.; Lin, K.; Ho, K. Y.; Teh, M.; Yeoh, K. G.; So, J. B. Y.; Huang, Z. Characterizing Variability in in Vivo Raman Spectra of Different Anatomical Locations in the Upper Gastrointestinal Tract toward Cancer Detection. *J. Biomed. Opt.* **2011**, *16* (3), 037003.
(40) De Gussem, K.; Vandenabeele, P.; Verbeken, A.; Moens, L. Raman Spectroscopic Study of Lactarius Spores (Russulales, Fungi). *Spectrochim. Acta A Mol. Biomol. Spectrosc.* **2005**, *61* (13−14), 2896−2908.
(41) Pence, I.; Mahadevan-Jansen, A. Clinical Instrumentation and Applications of Raman Spectroscopy. *Chem. Soc. Rev.* **2016**, *45* (7), 1958−1979.
(42) Benecky, M. J.; Copeland, R. A.; Rava, R. P.; Feldhaus, R.; Scott, R. D.; Metzler, C. M.; Metzler, D. E.; Spiro, T. G. Resonance Raman Spectra of the Pyridoxal Coenzyme in Aspartate Aminotransferase. Evidence for Pyridine Protonation and a Novel Photochemical H/D Exchange at the Imine Carbon Atom. *J. Biol. Chem.* **1985**, *260* (21), 11671−11678.
(43) Nagatomo, S.; Nagai, M.; Shibayama, N.; Kitagawa, T. Differences in Changes of the A1-B2 Subunit Contacts between Ligand Binding to the α and β Subunits of Hemoglobin A: UV

https://doi.org/10.1021/acsnano.2c00538
ACS Nano 2022, 16, 6426−6436

Resonance Raman Analysis Using Ni- Fe Hybrid Hemoglobin. *Biochemistry* **2002**, *41* (31), 10010−10020.
(44) Wang, C.; Neugebauer, U.; Bürck, J.; Myllykoski, M.; Baumgärtel, P.; Popp, J.; Kursula, P. Charge Isomers of Myelin Basic Protein: Structure and Interactions with Membranes, Nucleotide Analogues, and Calmodulin. *PLoS One* **2011**, *6* (5), No. e19915.
(45) Shah, N. C.; Lyandres, O.; Walsh, J. T.; Glucksberg, M. R.; Van Duyne, R. P. Lactate and Sequential Lactate- Glucose Sensing Using Surface-Enhanced Raman Spectroscopy. *Anal. Chem.* **2007**, *79* (18), 6927−6932.
(46) Pézolet, M.; Pigeon, M.; Ménard, D.; Caillé, J. P. Raman Spectroscopy of Cytoplasmic Muscle Fiber Proteins. Orientational Order. *Biophys. J.* **1988**, *53* (3), 319−325.
(47) Rygula, A.; Majzner, K.; Marzec, K. M.; Kaczor, A.; Pilarczyk, M.; Baranska, M. Raman Spectroscopy of Proteins: A Review: Raman Spectroscopy of Proteins. *J. Raman Spectrosc.* **2013**, *44* (8), 1061−1076.
(48) Thomas, G. J., Jr; Prescott, B.; Hamilton, M. G. Raman Spectra and Conformational Properties of Ribosomes during Various Stages of Disassembly. *Biochemistry* **1980**, *19* (15), 3604−3613.
(49) Tefelski, D. B.; Jastrzębski, C.; Wierzbicki, M.; Siegoczyński, R. M.; Rostocki, A. J.; Wieja, K.; Kościesza, R. Raman Spectroscopy of Triolein under High Pressures. *High Press. Res.* **2010**, *30* (1), 124−129.
(50) Ryzhikova, E.; Kazakov, O.; Halamkova, L.; Celmins, D.; Malone, P.; Molho, E.; Zimmerman, E. A.; Lednev, I. K. Raman Spectroscopy of Blood Serum for Alzheimer's Disease Diagnostics: Specificity Relative to Other Types of Dementia. *J. Biophotonics* **2015**, *8* (7), 584−596.
(51) Kurouski, D.; Van Duyne, R. P.; Lednev, I. K. Exploring the Structure and Formation Mechanism of Amyloid Fibrils by Raman Spectroscopy: A Review. *Analyst* **2015**, *140* (15), 4967−4980.
(52) Cowan, C. M.; Quraishe, S.; Hands, S.; Sealey, M.; Mahajan, S.; Allan, D. W.; Mudher, A. Rescue from Tau-Induced Neuronal Dysfunction Produces Insoluble Tau Oligomers. *Sci. Rep.* **2015**, *5*, 17191.
(53) Buividas, R.; Dzingelevičius, N.; Kubiliūtė, R.; Stoddart, P. R.; Khanh Truong, V.; Ivanova, E. P.; Juodkazis, S. Statistically Quantified Measurement of an Alzheimer's Marker by Surface-Enhanced Raman Scattering. *J. Biophotonics* **2015**, *8* (7), 567−574.
(54) Short, K. W.; Carpenter, S.; Freyer, J. P.; Mourant, J. R. Raman Spectroscopy Detects Biochemical Changes Due to Proliferation in Mammalian Cell Cultures. *Biophys. J.* **2005**, *88* (6), 4274−4288.
(55) Krafft, C.; Sobottka, S. B.; Schackert, G.; Salzer, R. Near Infrared Raman Spectroscopic Mapping of Native Brain Tissue and Intracranial Tumors. *Analyst* **2005**, *130* (7), 1070−1077.
(56) Krafft, C.; Neudert, L.; Simat, T.; Salzer, R. Near Infrared Raman Spectra of Human Brain Lipids. *Spectrochim. Acta A Mol. Biomol. Spectrosc.* **2005**, *61* (7), 1529−1535.
(57) Huang, S.; Ling, X.; Liang, L.; Song, Y.; Fang, W.; Zhang, J.; Kong, J.; Meunier, V.; Dresselhaus, M. S. Molecular Selectivity of Graphene-Enhanced Raman Scattering. *Nano Lett.* **2015**, *15* (5), 2892−2901.
(58) Silver, A.; Kitadai, H.; Liu, H.; Granzier-Nakajima, T.; Terrones, M.; Ling, X.; Huang, S. Chemical and Bio Sensing Using Graphene-Enhanced Raman Spectroscopy. *Nanomaterials (Basel)* **2019**, *9* (4), 516.
(59) Ling, X.; Huang, S.; Deng, S.; Mao, N.; Kong, J.; Dresselhaus, M. S.; Zhang, J. Lighting up the Raman Signal of Molecules in the Vicinity of Graphene Related Materials. *Acc. Chem. Res.* **2015**, *48* (7), 1862−1870.
(60) Huang, S.; Pandey, R.; Barman, I.; Kong, J.; Dresselhaus, M. Raman Enhancement of Blood Constituent Proteins Using Graphene. *ACS Photonics* **2018**, *5* (8), 2978−2982.
(61) Chen, S.; Wu, Q.; Mishra, C.; Kang, J.; Zhang, H.; Cho, K.; Cai, W.; Balandin, A. A.; Ruoff, R. S. Thermal Conductivity of Isotopically Modified Graphene. *Nat. Mater.* **2012**, *11* (3), 203−207.
(62) Balandin, A. A. Thermal Properties of Graphene and Nanostructured Carbon Materials. *Nat. Mater.* **2011**, *10* (8), 569−581.
(63) Chen, T.; Guestrin, C. XGBoost: A Scalable Tree Boosting System. *Proceedings of the 22nd ACM SIGKDD International Conference on Knowledge Discovery and Data Mining*; Association for Computing Machinery: New York, 2016; pp 785−794.
(64) Prokhorenkova, L.; Gusev, G.; Vorobev, A.; Dorogush, A. V.; Gulin, A. CatBoost: Unbiased Boosting with Categorical Features. *arXiv* 2017, 1706.09516. https://arxiv.org/abs/1706.09516 (accessed 2022-03-16).
(65) Hensley, K.; Hall, N.; Subramaniam, R.; Cole, P.; Harris, M.; Aksenov, M.; Aksenova, M.; Gabbita, S. P.; Wu, J. F.; Carney, J. M. Brain Regional Correspondence between Alzheimer's Disease Histopathology and Biomarkers of Protein Oxidation. *J. Neurochem.* **1995**, *65* (5), 2146−2156.
(66) van der Maaten, L. Visualizing Data Using T-SNE. *Journal of Machine Learning Research* **2008**, *9*, 2579−2605.
(67) Bamburg, J. R.; Bernstein, B. W. Actin Dynamics and Cofilin-Actin Rods in Alzheimer Disease. *Cytoskeleton* **2016**, *73* (9), 477−497.
(68) Banks, W. A.; Farr, S. A.; Salameh, T. S.; Niehoff, M. L.; Rhea, E. M.; Morley, J. E.; Hanson, A. J.; Hansen, K. M.; Craft, S. Triglycerides Cross the Blood-Brain Barrier and Induce Central Leptin and Insulin Receptor Resistance. *Int. J. Obes.* **2018**, *42* (3), 391−397.
(69) Chan, R. B.; Oliveira, T. G.; Cortes, E. P.; Honig, L. S.; Duff, K. E.; Small, S. A.; Wenk, M. R.; Shui, G.; Di Paolo, G. Comparative Lipidomic Analysis of Mouse and Human Brain with Alzheimer Disease. *J. Biol. Chem.* **2012**, *287* (4), 2678−2688.
(70) Johnson, L. A.; Zuloaga, K. L.; Kugelman, T. L.; Mader, K. S.; Morré, J. T.; Zuloaga, D. G.; Weber, S.; Marzulla, T.; Mulford, A.; Button, D.; Lindner, J. R.; Alkayed, N. J.; Stevens, J. F.; Raber, J. Amelioration of Metabolic Syndrome-Associated Cognitive Impairments in Mice via a Reduction in Dietary Fat Content or Infusion of Non-Diabetic Plasma. *EBioMedicine* **2016**, *3*, 26−42.
(71) Whiley, L.; Sen, A.; Heaton, J.; Proitsi, P.; García-Gómez, D.; Leung, R.; Smith, N.; Thambisetty, M.; Kloszewska, I.; Mecocci, P.; Soininen, H.; Tsolaki, M.; Vellas, B.; Lovestone, S.; Legido-Quigley, C. AddNeuroMed Consortium. Evidence of Altered Phosphatidylcholine Metabolism in Alzheimer's Disease. *Neurobiol. Aging* **2014**, *35* (2), 271−278.
(72) Higgins, J. P.; Flicker, L. Lecithin for Dementia and Cognitive Impairment. *Cochrane Database Syst. Rev.* **2000**, *4*, CD001015.
(73) Bélanger, M.; Allaman, I.; Magistretti, P. J. Brain Energy Metabolism: Focus on Astrocyte-Neuron Metabolic Cooperation. *Cell Metab.* **2011**, *14* (6), 724−738.
(74) Bass, B.; Upson, S.; Roy, K.; Montgomery, E. L.; Jalonen, T. O.; Murray, I. V. J. Glycogen and Amyloid-Beta: Key Players in the Shift from Neuronal Hyperactivity to Hypoactivity Observed in Alzheimer's Disease? *Neural Regeneration Res.* **2015**, *10* (7), 1023−1025.
(75) Parker, W. D., Jr; Filley, C. M.; Parks, J. K. Cytochrome Oxidase Deficiency in Alzheimer's Disease. *Neurology* **1990**, *40* (8), 1302−1303.
(76) Cardoso, S. M.; Proença, M. T.; Santos, S.; Santana, I.; Oliveira, C. R. Cytochrome c Oxidase Is Decreased in Alzheimer's Disease Platelets. *Neurobiol. Aging* **2004**, *25* (1), 105−110.
(77) Oakley, H.; Cole, S. L.; Logan, S.; Maus, E. Intraneuronal β-Amyloid Aggregates, Neurodegeneration, and Neuron Loss in Transgenic Mice with Five Familial Alzheimer's Disease Mutations: Potential Factors in Amyloid Plaque Formation. *J. Neurosci.* **2006**, *26*, 10129.
(78) Youmans, K. L.; Tai, L. M.; Kanekiyo, T.; Stine, W. B., Jr; Michon, S.-C.; Nwabuisi-Heath, E.; Manelli, A. M.; Fu, Y.; Riordan, S.; Eimer, W. A.; Binder, L.; Bu, G.; Yu, C.; Hartley, D. M.; LaDu, M. J. Intraneuronal Aβ Detection in 5xFAD Mice by a New Aβ-Specific Antibody. *Mol. Neurodegener.* **2012**, *7*, 8.

https://doi.org/10.1021/acsnano.2c00538
ACS Nano 2022, 16, 6426−6436

(79) Liang, Y.; Raven, F.; Ward, J. F.; Zhen, S.; Zhang, S.; Sun, H.; Miller, S. J.; Choi, S. H.; Tanzi, R. E.; Zhang, C. Upregulation of Alzheimer's Disease Amyloid-β Protein Precursor in Astrocytes Both in Vitro and in Vivo. *J. Alzheimers. Dis.* **2020**, *76* (3), 1071−1082.
(80) Choi, S. H.; Bylykbashi, E.; Chatila, Z. K.; Lee, S. W.; Pulli, B.; Clemenson, G. D.; Kim, E.; Rompala, A.; Oram, M. K.; Asselin, C.; Aronson, J.; Zhang, C.; Miller, S. J.; Lesinski, A.; Chen, J. W.; Kim, D. Y.; van Praag, H.; Spiegelman, B. M.; Gage, F. H.; Tanzi, R. E. Combined Adult Neurogenesis and BDNF Mimic Exercise Effects on Cognition in an Alzheimer's Mouse Model. *Science* **2018**, *361* (6406), DOI: 10.1126/science.aan8821.
(81) Howley, T.; Madden, M. G.; O'Connell, M.-L.; Ryder, A. G. The Effect of Principal Component Analysis on Machine Learning Accuracy with High Dimensional Spectral Data. *Applications and Innovations in Intelligent Systems XIII*; Springer London: London, 2006; pp 209−222.
(82) Smola, A. J.; Schölkopf, B. *Learning with Kernels*; Citeseer: Berlin, 1998; Vol. *4*.
(83) Buitinck, L.; Louppe, G.; Blondel, M.; Pedregosa, F.; Mueller, A.; Grisel, O.; Niculae, V.; Prettenhofer, P.; Gramfort, A.; Grobler, J.; Layton, R.; Vanderplas, J.; Joly, A.; Holt, B.; Varoquaux, G. API Design for Machine Learning Software: Experiences from the Scikit-Learn Project. *arXiv* **2013**, 1309.0238. https://arxiv.org/abs/1309.0238 (accessed 2022-03-16).
(84) Benesty, J.; Chen, J.; Huang, Y.; Cohen, I. Pearson Correlation Coefficient. In *Noise Reduction in Speech Processing*; Cohen, I., Huang, Y., Chen, J., Benesty, J., Eds.; Springer Berlin Heidelberg: Berlin, Heidelberg, 2009; pp 1−4.
(85) Roliński, T.; Gawinkowski, S.; Kamińska, A.; Waluk, J. Raman Spectra of Solid Amino Acids: Spectral Correlation Analysis as the First Step Towards Identification by Raman Spectroscopy. In *Optical Spectroscopy and Computational Methods in Biology and Medicine*; Baranska, M., Ed.; Springer Netherlands: Dordrecht, 2014; pp 329−354.

https://doi.org/10.1021/acsnano.2c00538
ACS Nano 2022, 16, 6426−6436